The Journal of Eukaryotic Microbiology

ISOP Published by the International Society of Protistologists

Journal of Eukaryotic Microbiology ISSN 1066-5234

ORIGINAL ARTICLE

Ultrastructural Changes of the Mitochondrion During the Life Cycle of *Trypanosoma brucei*

Tomáš Bílý[a,1], Shaghayegh Sheikh[a,1], Adeline Mallet[b,c], Philippe Bastin[b], David Pérez-Morga[d], Julius Lukeš[a,1] & Hassan Hashimi[a,1]

a Institute of Parasitology, Biology Center, Czech Academy of Sciences & Faculty of Science, University of South Bohemia, České Budějovice, Czech Republic

b Trypanosome Cell Biology Unit & INSERM U1201, Institut Pasteur, Paris, France

c Ultrastructural Bio Imaging Unit, C2RT, Institut Pasteur & Sorbonne Université école doctorale complexité du vivant, ED 515, Paris, France

d Laboratory of Molecular Parasitology, IBMM & Center for Microscopy and Molecular Imaging, Université Libre de Bruxelles, Brussels, Belgium

Keywords

Cristae; kinetoplastid; mitochondria; tomography.

Correspondence

Hassan Hashimi and Julius Lukeš, Institute of Parasitology, Biology CenterAQ1, Czech Academy of Sciences & Faculty of Science, University of South Bohemia, České Budějovice 370 05, Czech Republic;
Telephone number: +420 387775481;
FAX number: +420 385310388(HH);
Telephone no: +420 387775416;
FAX number: +420 385310388(JL)
e-mails: hassan@paru.cas.cz (HH) and jula@paru.cas.cz (JL)

Received: 18 November 2020; revised 4 February 2021; accepted February 15, 2021. Early View publication 19 March, 2021

doi:10.1111/jeu.12846

[1]Equal contribution.

ABSTRACT

The mitochondrion is crucial for ATP generation by oxidative phosphorylation, among other processes. Cristae are invaginations of the mitochondrial inner membrane that house nearly all the macromolecular complexes that perform oxidative phosphorylation. The unicellular parasite *Trypanosoma brucei* undergoes during its life cycle extensive remodeling of its single mitochondrion, which reflects major changes in its energy metabolism. While the bloodstream form (BSF) generates ATP exclusively by substrate-level phosphorylation and has a morphologically highly reduced mitochondrion, the insect-dwelling procyclic form (PCF) performs oxidative phosphorylation and has an expanded and reticulated organelle. Here, we have performed high-resolution 3D reconstruction of BSF and PCF mitochondria, with a particular focus on their cristae. By measuring the volumes and surface areas of these structures in complete or nearly complete cells, we have found that mitochondrial cristae are more prominent in BSF than previously thought and their biogenesis seems to be maintained during the cell cycle. Furthermore, PCF cristae exhibit a surprising range of volumes in situ, implying that each crista is acting as an independent bioenergetic unit. Cristae appear to be particularly enriched in the region of the organelle between the nucleus and kinetoplast, the mitochondrial genome, suggesting this part has distinctive properties.

TRYPANOSOMA brucei is the causative agent of human African trypanosomiasis and the veterinarian disease nagana (Barrett et al. 2003). This flagellated eukaryote undergoes a complex life cycle involving differentiation into specifically adapted stages as it alternates between the tsetse fly vector and the mammalian host (Vickerman 1985), allowing it to occupy various ecological niches. The single mitochondrion of *T. brucei* is drastically remodeled to meet the different bioenergetic requirements of each life cycle stage (Doleželová et al. 2020).

The *T. brucei* life cycle stage residing in the tsetse fly midgut is called the procyclic form (PCF) and contains a reticulated mitochondrion replete with disk-like cristae (Verner et al. 2015). In all aerobic eukaryotes, these prominent invaginations of the inner mitochondrial membrane house the respiratory chain protein complexes responsible for oxidative phosphorylation (Mannella 2020; Pánek et al. 2020). Thus, the organelle's ultrastructure is a manifestation of its active role in coupling catabolism of proline, the main carbon source for the citric acid cycle, with the production of cellular ATP.

In contrast, the *T. brucei* long slender bloodstream form (BSF), which proliferates preferentially in the mammalian blood, has a morphologically reduced mitochondrion compared to that of the PCF (Vickerman 1985). In the BSF, the organelle assumes a tubular shape that extends along the side of the cell opposite to the attached flagellum and has only few extensions and loops (Barrett et al. 2003; Hughes et al. 2017; Jakob et al. 2016), distinguishing it from the elaborately reticulated mitochondrion of the PCF.

Moreover, the rarely observed small cristae of the BSF mitochondrion (Brown et al. 1973) assume the tubulovesicular morphotype, whereas the prominent and abundant cristae in the PCF have a characteristic disk-like shape (Pánek et al. 2020). The ultrastructure of the BSF mitochondrion reflects that oxidative phosphorylation is suppressed in this life stage, with cellular ATP being produced exclusively by aerobic glycolysis (Verner et al. 2015). However, the mitochondrial DNA of *T. brucei*, which is a network composed of mutually interlocked circles, here termed the kinetoplast (k) DNA, assumes in the BSF and PCF identical morphology of a disk-shaped structure (Jensen and Englund 2012).

By using focused ion beam–scanning electron microscopy (FIB-SEM), we reconstructed the three-dimensional (3D) structure of the entire mitochondrion in the in vitro cultured monomorphic BSF (i.e. cells that have lost the capacity to differentiate into true PCF due to prolonged culturing) and PCF cells, of which other morphological features have already been analyzed using this approach (Bertiaux et al. 2018; Fontaine et al. 2017). Moreover, in both life cycle stages, we have analyzed in detail their cristae and kDNA, as well as the volume and surface area of these structures and have performed their comparative analysis.

MATERIALS AND METHODS

Focused ion beam–scanning electron microscope imaging and culturing of bloodstream form *Trypanosoma brucei*

Monomorphic bloodstream stage *T. brucei* strain 328–114 was grown in HMI9 supplemented with 10% fetal bovine serum, 10% Serum Plus at 37 °C in 5% CO_2. Trypanosomes in suspension in culture medium were quickly mixed in fixative (2% PFA, Applichem, Darmstadt, Germany), 2.5% glutaraldehyde (Electron Microscopy Sciences, EMS, Hatfield, PA) in 0.15 M sodium cacodylate (Sigma-Aldrich, St. Louis, MO) buffer, pH 7.4 at room temperature for 30 min. Fixative was removed by washing 5 × 3 min in 0.15 M cacodylate buffer, and samples were incubated in 1% osmium (OsO_4, EMS), 1.5% potassium ferrocyanide (Sigma-Aldrich) in 0.15 M cacodylate buffer for 40 min at room temperature. This was immediately followed by a second incubation in OsO_4 (1% osmium in double distilled H_2O (dd H_2O)) for 40 min at room temperature. After washing in dd H_2O for 5 × 3 min, samples were incubated overnight at 4 °C in 1% uranyl acetate (EMS). Uranyl acetate was removed by washing in dd H_2O for 5 × 3 min, serially dehydrated in increasing ethanol concentrations, embedded in agar 100 (Agar Scientific Ltd, Stansted, UK), and left to polymerize for 2 days at 60 °C. Embedded samples were then mounted on aluminum s.e.m. stubs (diameter 12 mm) and coated with B8 nm of platinum (Quorum Q150T ES). Focused ion beam–scanning electron microscope imaging was performed using a Zeiss Auriga Crossbeam system with Atlas3D software. The focused ion beam was set to remove 5-nm sections by propelling gallium ions at the surface after deposition of a protective Pt° layer. Imaging was done at 1.5 kV using an ESB (back-scattered electron) detector. 2516 slices were collected, representing a volume of 20.44 (width) × 12.8250 (height) × 12.58 (depth) μm, at 200 pixels/μm and voxel size: 0.005 × 0.005 × 0.005 μm^3. Alignments were automatically performed by the Atlas3D software.

Focused ion beam–scanning electron microscope imaging of procyclic form *Trypanosoma brucei*

For EM sample preparation, procyclic *T. brucei* strain 427 cells were fixed directly in SDM-79 medium at 27 °C with a final concentration of 2.5% glutaraldehyde (Sigma-Aldrich). Fixed samples were washed three times by the addition of 0.1 M cacodylate buffer (pH 7.2) buffer and postfixed in 1% osmium (EMS) in 0.1 M cacodylate buffer (pH 7.2) enriched with 1.5% potassium ferrocyanide (Sigma-Aldrich) for 1 h. After 3 washes in water, samples were incubated for 1 h in 1% tannic acid and postfixed a second time in 1% osmium. Samples were gradually dehydrated in acetone (Sigma-Aldrich) series from 50% to 100%. Cells were embedded in PolyBed812 resin (EMS) followed by polymerization for 48 h at 60 °C. For FIB-SEM analysis, the resin embedded cells were mounted on aluminum stubs, with the pyramidal surface of the resin block pointing upwards. The block surface was coated with a 20 nm thick layer gold–palladium in a Gatan Ion Beam Coater 681 sputtering device and in additional 2 nm platinum layer using the gas injection system placed inside the Field Emission Scanning Electron Microscope (FESEM) Crossbeam Auriga (Carl Zeiss, Iena, Germany) workstation microscope chamber. The specimen stage was tilted at 54° with 5 mm working distance of the pole piece, at the coincidence point of the electron and the gallium beams. The milling conditions for the trench that allowed the view of the cross section were 10 nA at accelerating voltage of 30 kV. The fine polishing of the surface block was performed with 5 nA at 30 kV. For the slice series, 1 nA milling current was applied removing a 10 nm layer from the specimen block surface. Scanning EM images were recorded with an aperture of 60 μm in the high-current mode at 1.5 or 2 kV of the in-lens EsB detector with the EsB grid set to −500 V. The voxel size was 10 nm in *x*, *y*, and *z*. Back-scattered electron images were acquired using ATLAS 5 software (Carl Zeiss).

Focused ion beam–scanning electron microscopy and 3D structure analysis

Conditions and parameters for culturing and preparation of *T. brucei* BSF and PCF were described elsewhere (Bertiaux et al. 2018; Vanwalleghem et al. 2015). Tomograms were scanned at the isotropic resolution of 10 and 5 nm for PCF and BSF, respectively. All tomograms were filtered with 2D median filter by using ImageJ (Schneider et al. 2012) and analyzed in the Amira software package (ThermoFischer, Waltham, MA). The 3D-models of cristae

were made by manual masking, while other organelles were masked utilizing semi-automatic tools. Mitochondrial and cristae volumes were calculated from 3D models and statistically evaluated.

Mapping of cristae and mitochondria volumes was done along the longitudinal axis of the trypanosome cell. Twisted trypanosome cells were either straightened with flatten volume tool in IMOD (Kremer et al. 1996) software package and analyzed, or were divided into small parts that had one side almost parallel to the longitudinal cell axis and analyzed in this direction individually. Finally, the dependency of cristae and mitochondria volumes on the longitudinal position of trypanosome bodies was plotted and rolling averages with five data point window were rendered in Fig. 4.

RESULTS

Mitochondrial structure in bloodstream and procyclic forms

In order to render the 3D structure of the single mitochondrion, the BSF and PCF cells were subjected to FIB-SEM (Vanwalleghem et al. 2015). In the generated series of sequential electron micrographs (Z-stack images), we have focused on obtaining whole or nearly whole cells. Due to the stochastic nature of trypanosome orientation and limited area of milling that is an integral feature of the FIB-SEM technology, we were only able to find one complete and one almost complete cell for each life cycle stage (Fig. 1 and 2; Videos S1–S8). An almost complete cell is defined here as sampling from the anterior end to the (partially captured) kDNA in the extended region of the mitochondrion, which is located adjacent to the flagellar pocket. In total, we were able to capture one complete BSF (Fig. 1A, B and 2A) and PCF cell (Fig. 1D and 2D), termed BSF1 and PCF1, respectively. Also, of note is that BSF2, in which the kDNA has been sectioned only partially, also has two nucleoli (Fig. 1C, Video S3), a sign that this cell has been captured during early mitosis (Martínez-Calvillo et al. 2019; Nepomuceno-Mejía et al., 2018). Like BSF2, the rendered PCF2 mitochondrion also lacks a rendered kDNA (Fig. 1D and 2D); however, it only has a single nucleolus.

Our primary intention to analyze in detail 3D reconstructions of the dynamic mitochondrion of *T. brucei* BSF and PCF is somewhat mitigated by the small sample size, precluding any statistical validation, since we were only able to capture two complete/almost complete organelles for each life cycle stage. Therefore, we recognize that it is especially important to validate our data in comparison to other studies. Therefore, we measured kDNA volume and compared our findings with previous studies (Table 1). However, only one study we know of has used a 3D SEM method to reconstruct the organellar volume of whole BSF cells during the cell cycle utilizing the conceptually similar serial block-face scanning electron microscopy (SBEM) (Hughes et al. 2017). Our results agree with those from this study in terms of both mitochondrial and kDNA volumes (Table 1), strengthening our data. Thus, we are able to proceed with other measurements with a degree confidence that this small sample of cells is likely to be representative.

Differences in mitochondrial and crista characteristics between life cycle stages

The obtained 3D models of mitochondria allowed us to measure the volume and surface area of mitochondrial sub-compartments and reveal any quantifiable differences in the organelle between BSF and PCF (Table 2 and 3). The total mitochondrial volume in BSF is lower than in PCF, since in the former cells the value ranges between 0.9 and 1.5 μm^3, whereas the mitochondrion in the latter cells occupy 2.5–3 μm^3 (Table 2). This is in agreement with previous observations that the BSF mitochondrion is reduced (Brown et al. 1973), while the larger and reticulated mitochondrion in the PCF reflects the upregulation of the Krebs cycle and oxidative phosphorylation (Verner et al. 2015).

We next turned our attention to mitochondrial sub-compartments. The kDNA volume was not significantly different between the analyzed life cycle stages as expected (Jensen and Englund 2012) (Table 2). Closer inspection of the BSF mitochondria revealed the presence of numerous structures resembling cristae (Fig. 1B, C and 2A, B). These BSF cristae are reduced in size compared to those observed in PCF, with the former occupying about 10 times less volume than the latter (Table 2 and Fig. 3). Again, this is in agreement with the notion that the PCF mitochondria are replete with electron transport chain complexes III and IV (Verner et al. 2015; Zíková et al. 2017), which occur in cristae membranes (Mannella 2020; Pánek et al. 2020).

We next calculated the portion of mitochondrial volume occupied by cristae in two BSF and PCF trypanosomes (Table 2). Cristae volume in BSF1 and BSF2 was 1 and 2%, respectively. Given that BSF2 was captured during mitosis, it likely explains why it has a more voluminous mitochondrion with double the number of cristae as compared to BSF1. By contrast, PCF1 and PCF2 cristae occupied ~2–13% of the mitochondrial volume. These results were surprising for two reasons. Firstly, the crista-luminal volume of BSF2 and PCF1 represented 2.2% and 2.65% of the mitochondrial volume, respectively, which were unexpectedly similar values for the two life cycle stages. Secondly, the range of cristae volumes is strikingly different between PCF1 and PCF2, which is 2.65% and 12.96%, respectively, indicating that the PCF trypanosomes exhibit a wide range of cristae-luminal volume (Fig. 3).

Due to the significant difference between the cristae volumes in PCF1 and PCF2, we decided to further explore the variability of cristae in this life stage. To that end, we obtained volumetric data from sections of mitochondria in the proximity to the nucleus from 10 additional PCF cells (Table 4). We chose this region because it exhibits a consistent ratio of crista vs. mitochondrion volume, as

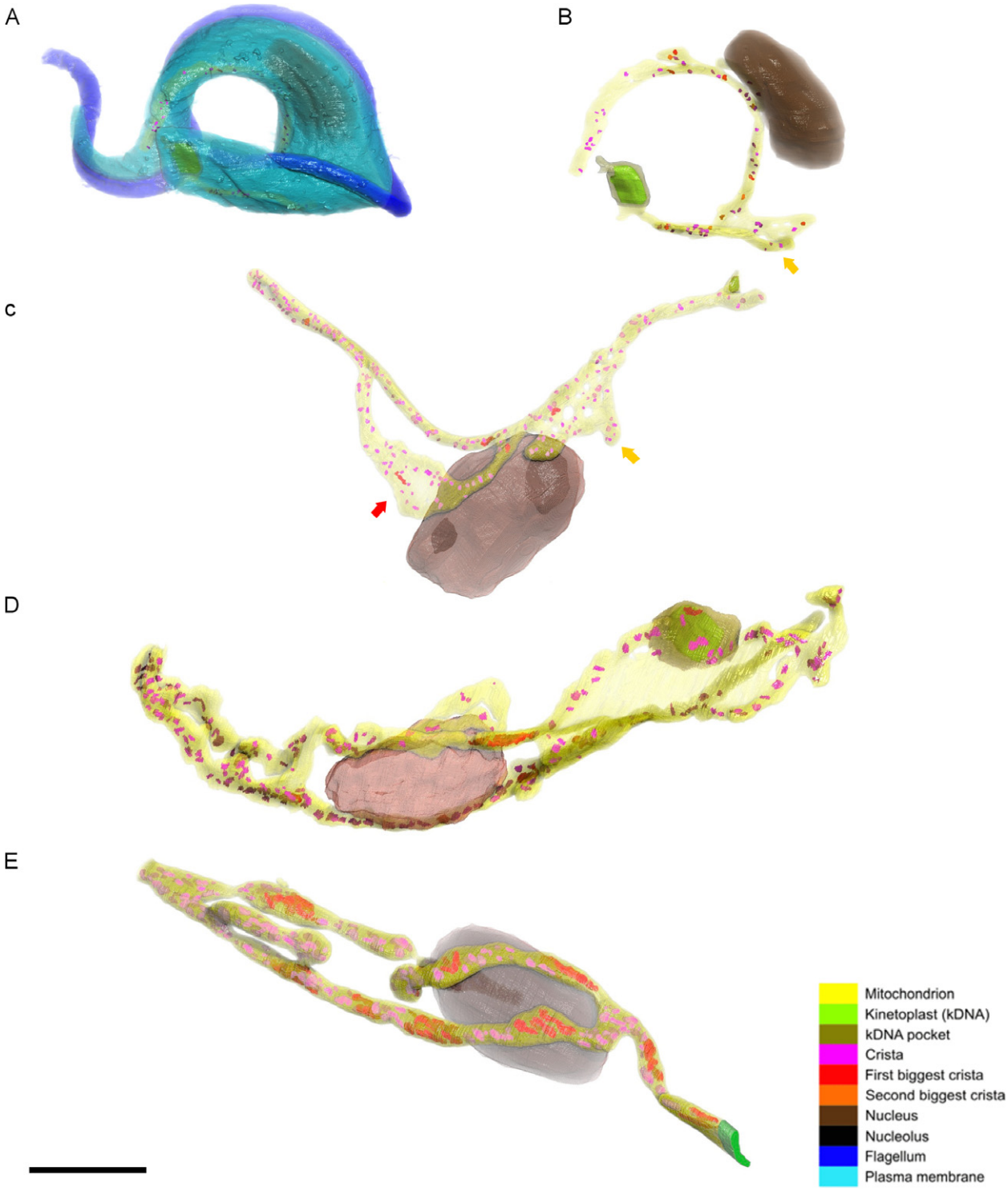

Figure 1 3D structure of mitochondrion from BSF and PCF *Trypanosoma brucei* whole or nearly complete cells. 3D architecture of mitochondrion and cristae in *T. brucei* visualized by FIB-SEM. The position of kinetoplast and nucleus is also depicted. Color key for rendered cellular structures given in key on bottom right, which includes color coding of cristae of different size classes. (**A**) BSF1 with plasma membrane; (**B**) BSF1 mitochondria and nucleus; (**C**) BSF2 mitochondria and nucleus (note two nucleoli in dark brown and lack of kDNA and the presence of a mitochondrial loop in anterior part of the cell as indicated by red arrow); (**D**) PCF1 mitochondria and nucleus; (**E**) PCF2 mitochondria and nucleus but missing complete kDNA. Yellow arrows in B and C point to branches extruding from mitochondrial region between kDNA and nucleus. Bottom left, 2,000 nm scale bar for all 3D structures.

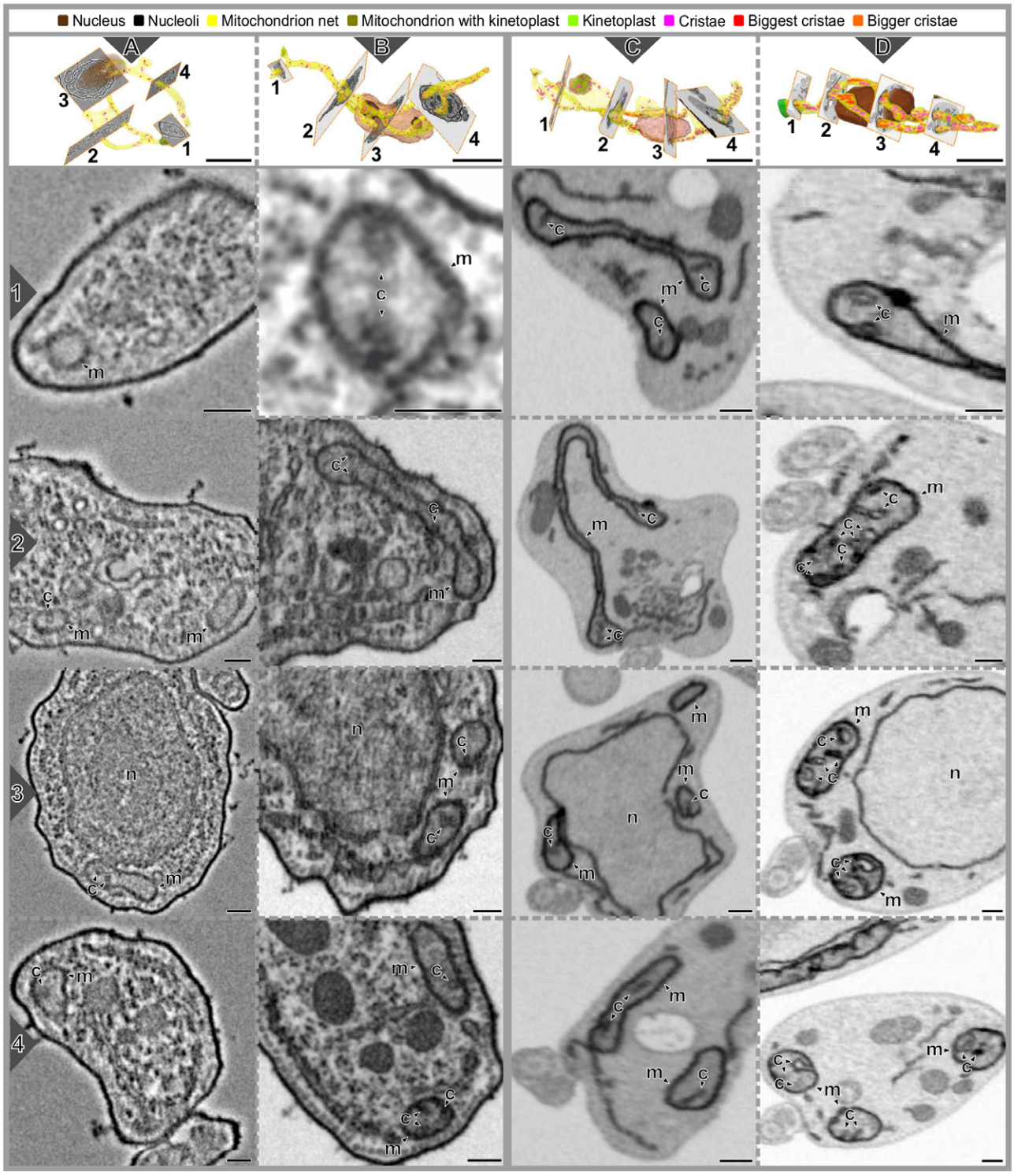

Figure 2 Representative sections of BSF and PCF *Trypanosoma brucei* whose mitochondria are reconstructed in Fig. 1. (**A**) BSF1; (**B**) BSF2; (**C**) PCF1; (**D**) PCF2. Top row shows 3D model and coordinates of each numbered slice 1–4 (indicated on left of each row). m, mitochondrion; c, crista. Scale bar for 3D model images is 2 μm and for tomogram virtual slices is 200 nm.

compared to other regions of the organelle (Fig. 4). This analysis revealed that cristae volume ranges from ~3% to 13% of total mitochondrial volume, well corresponding to the data from PCF1 and PCF2. Thus, it appears that the PCF trypanosomes exhibit a relatively wide range of crista volumes. Indeed, the standard deviation of crista volumes

Table 1. Comparison of BSF mitochondrial and kDNA volume from our study with previous studies

	Jakob et al. (2016)	Hughes et al. (2017)	Our study
Methods of mitochondria measurement	3D STED	SBF-SEM	FIB-SEM
Mitochondria volume (μm^3) ± standard deviation	2.828 ± 0.824	1.400 ± 0.490	1.200 ± 0.371
Methods of kDNA measurement	Not measured	SBF-SEM	FIB-SEM
kDNA volume (μm^3)	Not measured	0.050 ± 0.008	0.049

Standard deviations are provided when these data were available.

obtained in the whole cells is consistent with this notion. The populations of crista volumes measured in PCF1 and PCF2 exhibit a higher standard deviation in their volume compared to BSF1 and BSF2 (Fig. 3). This is also seen when the coefficient of variation (CV), a measure of dispersion of a population, is calculated for all the cells. PCF1 and PCF2 have $CV > 1$ whereas BSF1 and BSF2 have $CV < 1$, confirming that PCF cristae volumes exhibit a wider distribution. Interestingly, total cristae volume of PCF does not necessarily correlate with cristae number, as PCF2 has less but more voluminous cristae as compared to PCF1 (Table 2). In contrast, the BSF cristae volume and number are correlated with mitochondrial volume.

Next, we measured the surface area of cristae and "mitochondrial boundary membranes" (Table 3). We make the latter distinction to reflect that FIB-SEM requires membranes to be heavily stained to achieve high contrast, thus mingling the closely apposed outer and inner membranes in our images (Kizilyaprak et al. 2014; Steyer et al. 2020). Generally, the PCF mitochondrion has a greater surface area than the BSF organelle, which is in good correlation with it being reticulated as compared to the generally sausage-shaped mitochondrion of the BSF. However, PCF1 has a greater mitochondrial surface area of the two (near) complete cells despite having a smaller mitochondrial volume (Table 2 and 3), which may reflect more extensive reticulation (Fig. 1D, E). The surface area and volume of the two complete BSF mitochondria correlate, due to the simpler shape of the organelle and the bigger of the two (BSF2) being captured during early mitosis.

The surface area and volume of cristae correlate in all four (near) complete cells (Table 2 and 3). Furthermore, the mean surface area of the PCF1 and PCF2 cristae is six times higher than that of BSF1 and BSF2. This reflects a significant difference in the cristae shape between both forms, namely their disk-like shape in PCF versus the tubulovesicular one in BSF (Table 3). When considering the proportion of the inner mitochondrial membrane surface area (using the whole mitochondrial surface area as a proxy, since we were not able to fully delineate the inner and outer mitochondrial membranes), we observe that PCF generally has a higher proportion compared to BSF (36.45 ± 21.83 % vs. 10.98 ± 4.36 %).

Distinct features of the mitochondrial region between the nucleus and kDNA in procyclic form and evidence for crista biogenesis in bloodstream form

Finally, we have measured the crista-luminal and mitochondrial volumes, as well as the proportions of cristae along the anterior–posterior axis in the BSF and PCF cells with (almost) complete 3D reconstruction of their mitochondrion. The rolling averages (Fig. 4) show that in PCF, the mitochondrial region between the nucleus and the kDNA is particularly enriched in cristae volume (Fig. 4B). Indeed, the more voluminous cristae classes are concentrated in the region roughly between nucleus and kDNA. Such voluminous cristae occur infrequently in other regions of the organelle (Fig. 1D, E). Such a pattern was not observed in the BSF flagellates (Fig. 4A). However, in the analyzed BSF cells, isolated loops and branches emanating from the generally sausage-shaped mitochondrion were observed (Fig. 1B, C) that account for some of the locally increased volume of the mitochondrion (Fig. 4A). Interestingly, in BSF2, which is captured during early mitosis, an elaborate loop is observed in the part of the mitochondrion located in the anterior of the cell (Fig. 1C). Both BSF1 and BSF2 have additional branching of the mitochondrion in between the kDNA and nucleus (Fig. 1B, C). Furthermore, we note that cristae decorate the main tubule as well as these offshoots of in the BSF mitochondrion.

Table 2. Mitochondrial, crista, and kDNA volumes from BSF and PCF *Trypanosoma brucei*

Cell type	BSF1	BSF2	PCF1	PCF2
Mitochondrion (μm^3)	0.938	1.463	2.478	3.005
Cristae (μm^3)	1.150×10^{-2}	3.272×10^{-2}	6.757×10^{-2}	4.473×10^{-1}
[%] cristae/mitochondria volume	1.21	2.20	2.65	12.96
Mean	1.797×10^{5}	1.620×10^{5}	3.342×10^{5}	2.458×10^{6}
Standard deviation	8.577×10^{4}	1.108×10^{5}	4.980×10^{5}	5.564×10^{6}
Minimum (nm^3)	8.750×10^{2}	1.100×10^{4}	2.800×10^{4}	2.700×10^{4}
Maximum (nm^3)	4.565×10^{5}	8.287×10^{4}	6.502×10^{6}	4.074×10^{7}
Cristae number	64	202	214	182
kDNA volume (μm^3)	4.943×10^{-2}	Not doable	6.216×10^{-2}	Not doable

Table 3. Mitochondrial and crista surface areas from BSF and PCF *Trypanosoma brucei*

Cell type	BSF1	BSF2	PCF1	PCF2
Mitochondrion surface area (nm^2)	1.93×10^7	2.35×10^7	4.74×10^7	3.85×10^7
Cristae surface area (nm^2)	1.28×10^6	3.61×10^6	6.94×10^6	2.24×10^7
[%] cristae/ mitochondria surface area	6.62	15.34	14.62	58.27

DISCUSSION

We have built upon the classical study by Brown et al. (1973), which followed ultrastructural changes of the mitochondrion during the differentiation of *T. brucei* from the long slender BSF into PCF by employing conventional transmission electron microscopy. Here, we took advantage of the technological advance represented by FIB-SEM to compare how the BSF and PCF mitochondria differ from each other at high resolution, which allowed us to make 3D reconstructions of whole/nearly whole organelles and their sub-compartments.

Our primary intention to image whole organelles by FIB-SEM was complicated by the stochastic nature of data acquisition (Kizilyaprak et al. 2014). First of all, a very small area of the resin block (20–1,600 μm^2) containing the sample is defined by trenches and milled by the focus ion beam to image a depth in the 20–40 μm range. This results in a very small sampling volume in which the likelihood of capturing whole/nearly whole cells is considerably reduced. This problem is compounded by the cells assuming random orientations within the resin; as far as we know, there is no current technology and/or method that would somehow orient cell suspensions. Finally, while there is effort into choosing an appropriate region of interest (ROI) to mill, it is impossible to predict how the ROI will appear in subsequent deeper sections. However, the trade off this stochasticity is the superior resolution of the images. In contrast to other methods such as serial electron tomography, FIB-SEM has isotropic resolution and its automatic scanning eliminates artifacts and handling errors for a large number of sections. Thus, while our data lack statistical significance due to a small sample size, its high-resolution reconstruction of whole/nearly whole mitochondria does yield some qualitative insights.

The BSF mitochondrial volume has been previously measured *via* imaging indirect immunofluorescence of heat shock protein 70, an abundant matrix component, by super-resolution stimulated emission depletion microscopy (Jakob et al. 2016). As seen in Table 1, their measured volumes are larger than the volume derived from SEM studies. This is likely due to technical differences of the two methods, which each have their own advantages and trade-offs. Indirect immunofluorescence employs two IgG molecules to observe an antigen, adding a maximal theoretical distance of 17 nm (2 × 8.5 nm) length of an IgG (Tan et al. 2008) between the epitope and fluorophore. Among other factors, this would result in an increased volume measurement, which is indeed what was observed. On the other hand, this allows measuring whole cells on the slide, lending statistical power to the data. FIB-SEM allows high-resolution observation of the mitochondrion, yet due to the stochastic orientation of cells within the relatively small sectioned block fails to capture multiple whole cells. It should be noted that dehydration and resin polymerization steps during sample processing for electron microscopy may lead to some shrinkage, which further exacerbates differences in measured volumes listed in Table 1.

Unlike the aforementioned studies, we have measured the mitochondrial volume, surface area, and the parameters of cristae in both examined life cycle stages. While our results are in agreement with the general view regarding the structural remodeling and hence extensive plasticity of the organelle during differentiation from BSF to PCF (Böhringer and Hecker 1975; Brown et al. 1973; Ghiotto et al. 1979), our 3D reconstructions revealed several novel features. Although the presence of more elaborate cristae in PCF as compared to BSF was expected, we were surprised to see the wide distribution of cristae volumes recorded in two (nearly) whole PCF cells and 10 additional nucleus-proximal mitochondrial regions. This phenomenon can be explained by the previous observations that cristae from isolated mitochondria can expand and contract due to their bioenergetic state in vitro (Hackenbrock 1966; Mannella 2020). When respiration is artificially boosted by molar excess of ADP and inorganic phosphate, isolated mitochondria assume a "condensed" appearance with swollen crista lumina. Moreover, when these substrates are depleted, respiration switches into a resting state in which mitochondria assume an "orthodox" appearance where cristae look normal. This type of remodeling of cristae as a function of metabolic state has also been observed in human hepatocytes (Dlasková et al., 2019). Furthermore, each crista within a single human mitochondrion exhibits different membrane potential, a result of different energetic fluxes through respiratory chain complexes (Wolf et al. 2019). Thus, we speculate that the heterogeneity of cristae volumes in the PCF flagellates, which respire even in the presence of glucose (Horvath et al. 2005), is due to capturing individual crista in different respiration states. Certainly, the relative homogeneity of cristae volumes observed in BSF, which do not undergo oxidative phosphorylation, is consistent with this hypothesis. A substantial expansion of the inner mitochondrial surface area in PCF likely accommodates respiratory chain complexes that are expressed in this life cycle stage.

The enrichment of cristae volume in the region of the mitochondrion between the nucleus and kDNA observed in this study is potentially a novel feature. This observation is not likely to be an artifact as the chemical fix was added directly to the medium of PCF cells growing under standard culturing conditions (Bertiaux et al. 2018). We hypothesize that this aggregation of cristae may be an adaptation

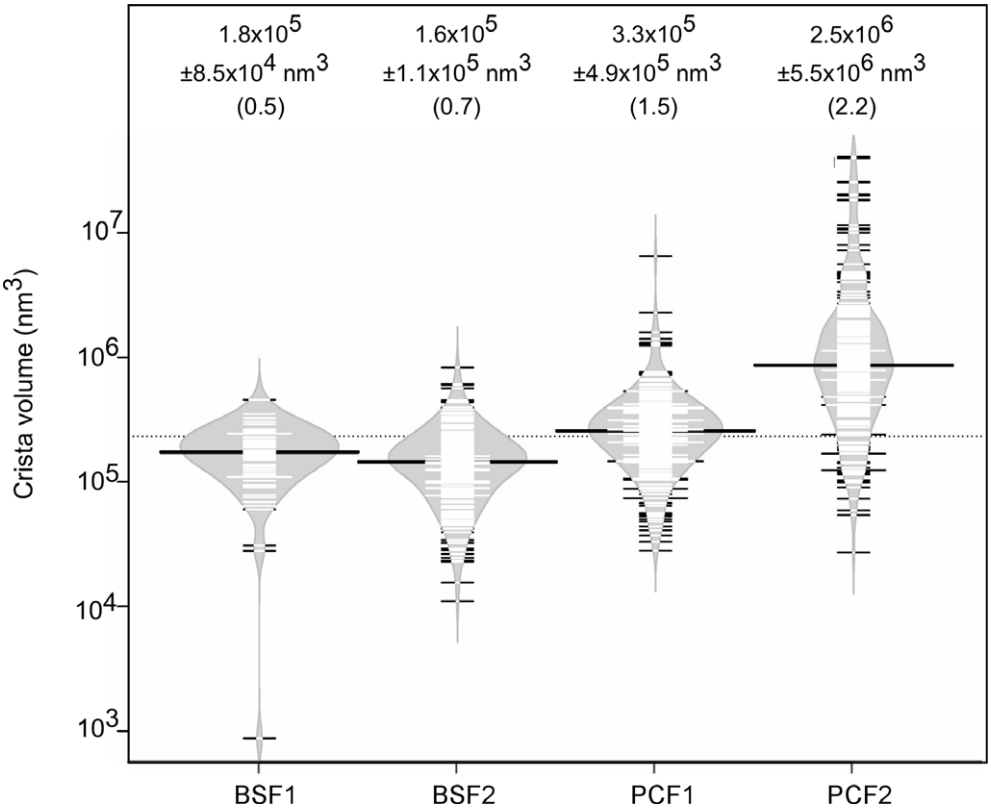

Figure 3 Crista volume distribution in BSF and PCF *Trypanosoma brucei* cells. Bean plot showing the cristae volume from individual BSF and PCF cells rendered in Fig. 1. *X*-axis cell, BSF and PCF cell designations; *y*-axis cristae volume (nm^3). Numbers on top of each cell are average volume of cristae ± standard deviation. Number in the parenthesis below is the coefficient of variation (CV) of each population, which is the ratio of the reported standard deviation and mean. The bold black lines in each bean plot indicate the mean. Thick black and white lines represent individual data points; longer lines show two or more data points with same value.

for meeting potentially higher energy demands in this part of the organelle due to the kDNA maintenance and expression (Jensen and Englund 2012; Verner et al. 2015) and/or the persistent active vesicular trafficking that occurs in the vicinity of the flagellar pocket (Zoltner et al. 2016). These explanations are consistent with our observation that such aggregation is not observed in BSF, whose mitochondria lack the oxidative phosphorylation pathway (Verner et al. 2015; Zíková et al. 2017). However, the region of the organelle between the nucleus and kDNA is still notable in BSF because branches emanating from here have been proposed to be part of mitochondrial division during the BSF cell cycle (Jakob et al. 2016). Furthermore, this part of the BSF mitochondrion is susceptible to fenestration upon treatment with trypanolytic factors (normal human serum or the apolipoprotein ApoL1) or RNAi depletion of trypanosome mitofusin-like protein (Fontaine et al. 2017; Vanwalleghem et al. 2015), which may signify a defect in mitochondrial division, as has been documented for the mitofusin-related protein DNM1 in yeast (Bleazard et al. 1999). Thus, this part of the mitochondrion may play a role in this process in PCF as well, possibly resulting in the larger cristae observed here.

Another unexpected result was the number of tubulovesicular cristae observed in the mitochondria of in vitro cultured BSF cells. The widely held view postulated that cristae are virtually absent from these organelles (Vickerman 1985), although few reports on their observation are available (Brown et al. 1973). We anticipated these structures to occur to a lesser extent than observed in the FIB-SEM data, and we certainly did not expect them to occupy up to 2% of the total mitochondrial volume and up to 15% of the organelle's total surface area. An artifact of the culture conditions of the BSF cells prior to observation (Vanwalleghem et al. 2015) is unlikely, since cristae in BSF have been observed in different strains and growing conditions (Brown et al. 1973; Ghiotto et al. 1979). Thus, we conclude that the observed diminished cristae are a genuine yet underestimated feature of the BSF mitochondria. This observation seems to correlate well with the recently reported protein-richness of this organelle, which is, against expectations, comparable to the 80% proteome of the PCF mitochondrion (Zíková et al. 2017).

Interestingly, we observe that the number of these cristae appears to double during mitosis, as can be seen from the comparison of BSF1 and BSF2 (Table 2). The biogenesis of cristae occurs in BSF. Supporting this idea is the

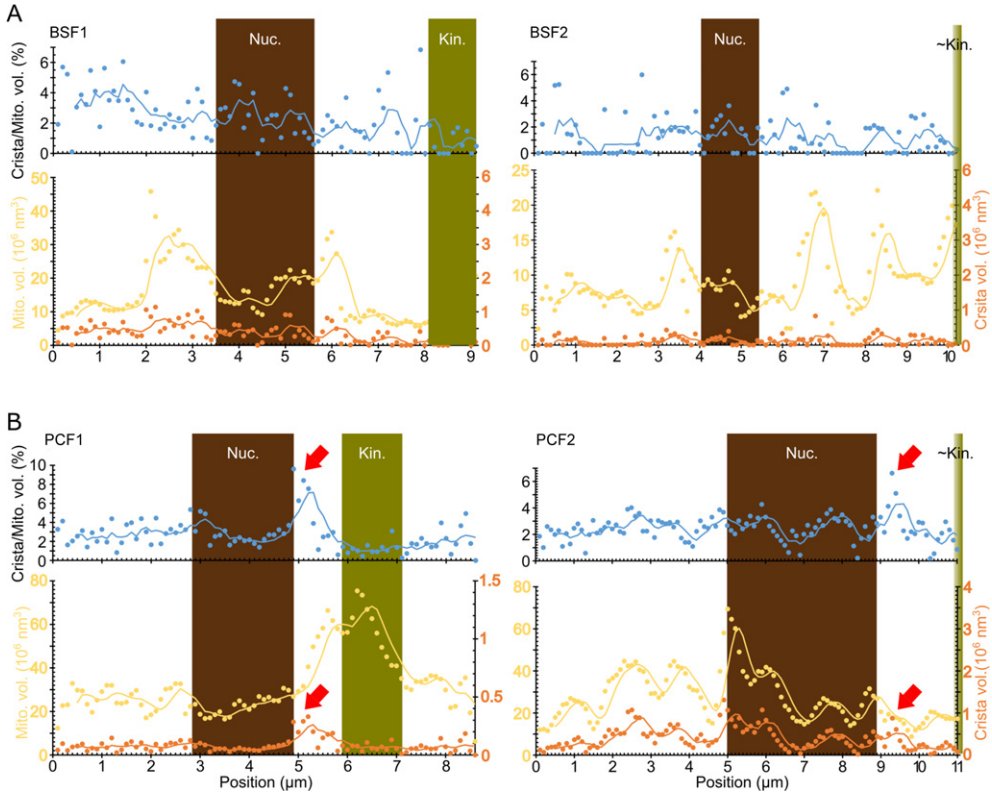

Figure 4 Mitochondria and crista volumes along the anterior–posterior axis of BSF and PCF *Trypanosoma brucei*. Top blue graph depicts crista mitochondrion volume in percentage for BSF (**A**) and PCF (**B**) cells along the anterior–posterior axis rendered in Fig. 1. Bottom graph shows mitochondrial volumes (yellow, scale on left) and crista volumes (orange, scale on right). Dots show data points recorded for every 200 nm section whereas lines are 5 data point rolling averages. Red arrows indicate the largest cristae volumes at the part of the mitochondrion between the nucleus (demarked in brown) and kDNA (dark green).

Table 4. Mitochondrial and crista volumes measured from 10 PCF near the nucleus

Mitochondrial volume (μm^3)	Crista volume (μm^3)	Crista/mitochondrial volume (%)
1.864×10^{-2}	2.924×10^{-3}	13.56
1.253×10^{-1}	1.854×10^{-2}	12.89
7.236×10^{-2}	8.723×10^{-3}	10.75
2.576×10^{-2}	2.814×10^{-3}	9.85
4.683×10^{-2}	3.882×10^{-3}	7.65
6.213×10^{-2}	4.474×10^{-3}	6.72
9.061×10^{-2}	5.626×10^{-3}	5.85
3.331×10^{-2}	2.064×10^{-3}	5.83
1.229×10^{-2}	6.810×10^{-4}	5.25
7.042×10^{-2}	2.256×10^{-3}	3.10
	Average ± standard deviation	8.14 ± 3.3

observation of conspicuous cristae in an anterior loop emanating from the main mitochondrial tubule of BSF2, captured in early mitosis and posterior branches observed in both BSF cells. Such structures have been previously observed and were hypothesized to be needed for mitochondrial division during the cell cycle (Jakob et al. 2016). This observation is consistent with the gross morphological changes to the organelle observed during the cell cycle in *Crithidia fasciculata*, a related, exclusively insect-infecting trypanosomatid (DiMaio et al. 2018). Indeed, in BSF2, the posterior branch and anterior loop appear to be coming together, a fusion step proposed to give rise to a second mitochondrial tubule needed for cell division. We speculate that these cristae may represent seeds for the formation of large disk-like cristae during differentiation into PCF. The possibility that they are remnants of the disk-like cristae from the previous insect forms is nullified by the fact that the analyzed strain of BSF *T. brucei* is monomorphic, incapable of complete differentiation, most likely due to extended in vitro passaging (Matthews and Gull 1994).

Above, we have disclosed the drawbacks of analyzing whole cells in the FIB-SEM data; however, with this method, we were able to measure cristae with high-resolution and without any artifacts due to sample preparation. Given the drawbacks of this method, sampling of a small number of whole/nearly whole cells has allowed us to reveal many interesting phenomena. The maintenance of cristae during the cell cycle in BSF, the heterogeneity of cristae volumes in PCF, especially their larger volumes seen between the kDNA and nucleus, would be difficult to observe in the random parts of incompletely rendered

cells. However, these observations should be considered with a modicum of caution since the small sample size precludes robust statistical analysis of these phenomena.

This study serves as a starting point for dissecting the steps involved in the disk-like cristae formation during the BSF to PCF differentiation. It also represents an interesting high-resolution picture of mitochondrial architecture in the two examined life cycle stages. The next step will be to tackle how the cristae-shaping proteins, such as those constituting the mitochondrial contact site and cristae organizing system, which facilitates negative curvature at the base of cristae (Dlasková et al., 2019; Hashimi 2019; Kaurov et al. 2018) and F_OF_1 ATP synthase dimers, which promotes positive curvature at crista rims (Mühleip et al. 2017), influence the formation of disk-like cristae.

ACKNOWLEDGMENTS

Czech Science Foundation grants 20-23513S, 20-07186S and 17-21409S, ERC CZ grant LL1601, Czech Ministry of Education OPVVV16_019/0000759, and Czech BioImaging grant LM2015062 and ERD Fund (003/0000441) to J.L. and H.H. supported this work. The "Action de Recherches Concertées" of the University of Brussels (ARC ADV), and the Fonds de la Recherche Scientifique (F.R.S.-FNRS, PDR T.0159.13) funded the laboratory of D.P.M. The Center for Microscopy and Molecular Imaging (CMMI-ULB) is supported by the European Regional Development Fund and Wallonia. A.M. and P.B. were funded by a French Government Investissement d'Avenir programme, Laboratoire d'Excellence (ANR-10-LABX-62-IBEID). We are also grateful for support for FESEM Zeiss Auriga equipment from the French Government Programme Investissement d'Avenir France BioImaging (FBI, N° ANR-10-INSB-04-01) and from a DIM-Malinf grant from the Région Ile-de-France.

LITERATURE CITED

Barrett, M. P., Burchmore, R. J., Stich, A., Lazzari, J. O., Frasch, A. C., Cazzulo, J. J. & Krishna, S. 2003. The trypanosomiases. *Lancet*, 362:1469–1480.

Bertiaux, E., Mallet, A., Fort, C., Blisnick, T., Bonnefoy, S., Jung, J., Lemos, M., Marco, S., Vaughan, S. & Trépout, S. 2018. Bidirectional intraflagellar transport is restricted to two sets of microtubule doublets in the trypanosome flagellum. *J. Cell Biol.*, 217:4284–4297.

Bleazard, W., McCaffery, J. M., King, E. J., Bale, S., Mozdy, A., Tieu, Q., Nunnari, J. & Shaw, J. M. 1999. The dynamin-related GTPase Dnm1 regulates mitochondrial fission in yeast. *Nat. Cell Biol.*, 1:298–304.

Böhringer, S. & Hecker, H. 1975. Quantitative ultrastructural investigations of the life cycle of *Trypanosoma brucei*: a morphometric analysis. *The Journal of Protozoology*, 22:463–467.

Brown, R. C., Evans, D. A. & Vickerman, K. 1973. Changes in oxidative metabolism and ultrastructure accompanying differentiation of the mitochondrion in *Trypanosoma brucei*. *Int. J. Parasitol.*, 3:691–704.

DiMaio, J., Ruthel, G., Cannon, J. J., Malfara, M. F. & Povelones, M. L. 2018. The single mitochondrion of the kinetoplastid parasite *Crithidia fasciculata* is a dynamic network. *PLoS One*, 13:e0202711.

Dlasková, A., Špaček, T., Engstová, H., Špačková, J., Schröfel, A., Holendová, B., Smolková, K., Plecitá-Hlavatá, L. & Ježek, P. 2019. Mitochondrial cristae narrowing upon higher 2-oxoglutarate load. *Biochim. Biophys. Acta Bioenerget.*, 1860(8):659–678.

Doleželová, E., Kunzová, M., Dejung, M., Levin, M., Panicucci, B., Regnault, C., Janzen, C. J., Barrett, M. P., Butter, F. & Zíková, A. 2020. Cell-based and multi-omics profiling reveals dynamic metabolic repurposing of mitochondria to drive developmental progression of *Trypanosoma brucei*. *PLoS Biol.*, 18: e3000741.

Fontaine, F., Lecordier, L., Vanwalleghem, G., Uzureau, P., Van Reet, N., Fontaine, M., Tebabi, P., Vanhollebeke, B., Büscher, P. & Pérez-Morga, D. 2017. APOLs with low pH dependence can kill all African trypanosomes. *Nat. Microbiol.*, 2:1500–1506.

Ghiotto, V., Brun, R., Jenni, L. & Hecker, H. 1979. *Trypanosoma brucei*: morphometric changes and loss of infectivity during transformation of bloodstream forms to procyclic culture forms in vitro. *Exp. Parasitol.*, 48:447–456.

Hackenbrock, C. R. 1966. Ultrastructural bases for metabolically linked mechanical activity in mitochondria. I. Reversible ultrastructural changes with change in metabolic steady state in isolated liver mitochondria. *J. Cell. Biol.*, 30:269–297.

Hashimi, H. 2019. A parasite's take on the evolutionary cell biology of MICOS. *PLoS Pathog.*, 15:e1008166.

Horvath, A., Horakova, E., Dunajcikova, P., Verner, Z., Pravdova, E., Slapetova, I., Cuninkova, L. & Lukes, J. 2005. Downregulation of the nuclear-encoded subunits of the complexes III and IV disrupts their respective complexes but not complex I in procyclic *Trypanosoma brucei*. *Mol. Microbiol.*, 58:116–130.

Hughes, L., Borrett, S., Towers, K., Starborg, T. & Vaughan, S. 2017. Patterns of organelle ontogeny through a cell cycle revealed by whole-cell reconstructions using 3D electron microscopy. *J. Cell Sci.*, 130:637–647.

Jakob, M., Hoffmann, A., Amodeo, S., Peitsch, C., Zuber, B. & Ochsenreiter, T. 2016. Mitochondrial growth during the cell cycle of *Trypanosoma brucei* bloodstream forms. *Sci. Rep.*, 6:1–13.

Jensen, R. E. & Englund, P. T. 2012. Network news: the replication of kinetoplast DNA. *Annu. Rev. Microbiol.*, 66:473–491.

Kaurov, I., Vancová, M., Schimanski, B., Cadena, L. R., Heller, J., Bílý, T., Potěšil, D., Eichenberger, C., Bruce, H., Oeljeklaus, S., Warscheid, B., Zdráhal, Z., Schneider, A., Lukeš, J. & Hashimi, H. 2018. The diverged trypanosome MICOS complex as a hub for mitochondrial cristae shaping and protein import. *Curr. Biol.*, 28:3393–3407 e5.

Kizilyaprak, C., Bittermann, A. G., Daraspe, J. & Humbel, B. M. 2014. FIB-SEM tomography in biology. *In:* Kuo, J. (ed.), Electron Microscopy: Methods and Protocols. Humana Press, Totowa, NJ. p. 541–558.

Kremer, J. R., Mastronarde, D. N. & McIntosh, J. R. 1996. Computer visualization of three-dimensional image data using IMOD. *J. Struct. Biol.*, 116:71–76.

Mannella, C. A. 2020. Consequences of folding the mitochondrial inner membrane. *Front. Physiol.*, 11:536.

Martínez-Calvillo, S., Florencio-Martínez, L. E. & Nepomuceno-Mejía, T. 2019. Nucleolar structure and function in trypanosomatid protozoa. *Cells*, 8:421.

Matthews, K. R. & Gull, K. 1994. Evidence for an interplay between cell cycle progression and the initiation of differentiation between life cycle forms of African trypanosomes. *J. Cell. Biol.*, 125:1147–1156.

Mühleip, A. W., Dewar, C. E., Schnaufer, A., Kühlbrandt, W. & Davies, K. M. 2017. In situ structure of trypanosomal ATP synthase dimer reveals a unique arrangement of catalytic subunits. *Proc. Natl Acad. Sci. USA*, 114:992–997.

Nepomuceno-Mejía, T., Florencio-Martínez, L. E. & Martínez-Calvillo, S. 2018. Nucleolar division in the promastigote stage of leishmania major parasite: a Nop56 point of view. *Biomed. Res. Int.*, 2018:1641839.

Pánek, T., Eliáš, M., Vancová, M., Lukeš, J. & Hashimi, H. 2020. Returning to the fold for lessons in mitochondrial crista diversity and evolution. *Curr. Biol.*, 30:R575–R588.

Schneider, C. A., Rasband, W. S. & Eliceiri, K. W. 2012. NIH Image to ImageJ: 25 years of image analysis. *Nat. Methods*, 9:671–675.

Steyer, A. M., Ruhwedel, T., Nardis, C., Werner, H. B., Nave, K.-A. & Möbius, W. 2020. Pathology of myelinated axons in the PLP-deficient mouse model of spastic paraplegia type 2 revealed by volume imaging using focused ion beam-scanning electron microscopy. *J. Struct. Biol.*, 210:107492.

Tan, Y. H., Liu, M., Nolting, B., Go, J. G., Gervay-Hague, J. & Liu, G.-Y. 2008. A nanoengineering approach for investigation and regulation of protein immobilization. *ACS Nano*, 2:2374–2384.

Vanwalleghem, G., Fontaine, F., Lecordier, L., Tebabi, P., Klewe, K., Nolan, D. P., Yamaryo-Botté, Y., Botté, C., Kremer, A. & Burkard, G. S. 2015. Coupling of lysosomal and mitochondrial membrane permeabilization in trypanolysis by APOL1. *Nat. Commun.*, 6:1–10.

Verner, Z., Basu, S., Benz, C., Dixit, S., Dobáková, E., Faktorová, D., Hashimi, H., Horáková, E., Huang, Z., Paris, Z., Pena-Diaz, P., Ridlon, L., Týč, J., Wildridge, D., Zíková, A. & Lukeš, J. 2015. Malleable mitochondrion of *Trypanosoma brucei*. *Int. Rev. Cell Mol. Biol.*, 315:73–151.

Vickerman, K. 1985. Developmental cycles and biology of pathogenic trypanosomes. *Br. Med. Bull.*, 41:105–114.

Wolf, D. M., Segawa, M., Kondadi, A. K., Anand, R., Bailey, S. T., Reichert, A. S., van der Bliek, A. M., Shackelford, D. B., Liesa, M. & Shirihai, O. S. 2019. Individual cristae within the same mitochondrion display different membrane potentials and are functionally independent. *EMBO J.*, 38:e101056.

Zíková, A., Verner, Z., Nenarokova, A., Michels, P. A. M. & Lukeš, J. 2017. A paradigm shift: the mitoproteomes of procyclic and bloodstream *Trypanosoma brucei* are comparably complex. *PLoS Pathog.*, 13:e1006679.

Zoltner, M., Horn, D., de Koning, H. P. & Field, M. C. 2016. Exploiting the Achilles' heel of membrane trafficking in trypanosomes. *Curr. Opin. Microbiol.*, 34:97–103.

SUPPORTING INFORMATION

Additional supporting information may be found online in the Supporting Information section at the end of the article.

Video S1. 3D model of bloodstream *T. brucei* BSF1 mitochondrion.

Video S2. Passage through the z-axis of bloodstream *T. brucei* BSF1 tomogram.

Video S3. 3D model of bloodstream *T. brucei* BSF2 mitochondrion.

Video S4. Passage through the z-axis of bloodstream *T. brucei* BSF2 tomogram.

Video S5. 3D model of procyclic *T. brucei* PCF1 mitochondrion.

Video S6. Passage through the z-axis of procyclic *T. brucei* PCF1 tomogram.

Video S7. 3D model of procyclic *T. brucei* PCF2 mitochondrion.

Video S8. Passage through the *z*-axis of procyclic *T. brucei* PCF2 tomogram.